Nanoscale Advances

ROYAL SOCIETY OF CHEMISTRY

PAPER

View Article Online
View Journal | View Issue

Cite this: *Nanoscale Adv.*, 2025, **7**, 6972

Impact of oil phase composition on the efficacy of nanoemulsions for verteporfin-mediated photodynamic therapy in ovarian cancer

Laura Fuentes Varela, [ag] María Emilia Vasquez,[a] Carmen Abuín Redondo, [a] Andrea Estrella Arias-Diaz, [ag] Miguel Abal, [ac] Clotilde Costa, [ac] Roberto Piñeiro, [ac] Irene Villa, [d] Ekaterina A. Kukushkina,[d] Lucia Lama,[h] Antía Cabezas,[g] Rafael López López *[abcefg] and Ana B. Dávila-Ibánez *[ac]

Nanomedicine has emerged as a powerful strategy to enhance both therapeutic efficacy and diagnostic precision in oncology. Among the various nanoscale platforms, nanoemulsions have shown promising potential as drug delivery systems, particularly in photodynamic therapy. However, the design of effective nanoemulsions requires careful consideration of multiple formulation parameters, especially the choice of the oil core, which remains insufficiently explored. In this study, we developed and compared two nanoemulsions differing only in their oil phase, oleic acid or miglyol, both loaded with the photosensitizer verteporfin, a clinically approved photosensitizer. We systematically evaluated their physicochemical characteristics, loading capacity, encapsulation efficiency, storage stability, and therapeutic efficacy in an ovarian cancer cell line. Our results demonstrate that the oil phase significantly influences nanoemulsion performance. Verteporfin-loaded miglyol-based nanoemulsions exhibited higher drug loading capacity, improved colloidal stability, and greater photodynamic cytotoxicity compared to the oleic acid-based counterpart. These findings underscore the critical role of formulation components in determining the functionality of nanocarriers and highlight the importance of rational nanoemulsion design to maximize therapeutic outcomes in photodynamic therapy and broader nanomedicine applications.

Received 20th May 2025
Accepted 10th August 2025

DOI: 10.1039/d5na00496a

rsc.li/nanoscale-advances

Introduction

Nanomedicine is revolutionizing biomedicine by providing next-generation tools for diagnostics and therapeutics, particularly for the treatment of complex diseases such as cancer. The unique physicochemical properties of nanomaterials, combined with their tunable surface characteristics, allow for the design of multifunctional theranostic platforms that outperform conventional clinical technologies.[1,2]

In this context, nanomaterials are increasingly being developed to address the limitations of conventional biomedical and clinical approaches. Both inorganic (*e.g.*, metals or metal oxides) and organic (*e.g.*, liposomes, polymeric nanoparticles) nanocarriers have been widely explored, each offering distinct advantages in biomedical applications, such as minimizing side effects, enhancing treatment efficacy, and overcoming drug resistance.[3–6]

Importantly, in oncology, nanoparticles have facilitated highly sensitive imaging and the development of targeted therapies, including photothermal and photodynamic approaches.[7–10]

Among nanocarriers, organic nanoparticles are preferred due to their biocompatibility, biodegradability, and low toxicity. Their chemical versatility enables surface modifications tailored to specific applications, enhancing targeting and drug delivery efficiency.[11–13] More specifically, lipid-based nanoparticles (LNPs) have achieved regulatory approval and clinical translation by the Food and Drug Administration (FDA)[14,15] and the European Medicines Agency (EMA) with formulations like Doxil®, Lipodox®, Onivyde®, Myocet®, demonstrating improved pharmacokinetics and targeted delivery that minimizes systemic toxicity.[16]

[a]*Translational Medical Oncology (Oncomet), Health Research Institute of Santiago (IDIS), Santiago de Compostela, Spain. E-mail: ana.belen.davila.ibanez@sergas.es*
[b]*Medical Oncology Department, Complexo Hospitalario Universitario de Santiago de Compostela (SERGAS), Santiago de Compostela, Spain*
[c]*CIBERONC, Centro de Investigación Biomédica en Red Cáncer, 28029 Madrid, Spain*
[d]*Department of Materials Science, University of Milano-Bicocca, 20125 Milano, Italy*
[e]*Galician Precision Oncology Research Group (ONCOGAL), Medicine and Dentistry, Spain*
[f]*Liquid Biopsy Analysis Unit, Translational Medical Oncology (Oncomet), Health Research Institute of Santiago (IDIS), Santiago de Compostela, Spain*
[g]*Universidade de Santiago de Compostela (USC), Santiago de Compostela, Spain*
[h]*Universidade de Coruña (UDC), A Coruña, Spain*

Within the LNP family, nanoemulsions (NEs), oil-in-water systems stabilized by surfactants, have emerged as promising carriers for poorly water-soluble drugs.[17]

By incorporating hydrophobic compounds into their oil core, NEs protect these agents from premature degradation, enable controlled release, and enhance both therapeutic efficacy and formulation stability.[18–20] Despite the confirmed feasibility of designing and synthesizing NE-based drug delivery systems, their success depends on several critical factors, including colloidal stability, encapsulation efficiency (EE%), and the physicochemical properties of the oil phase. These elements collectively influence drug loading, release profiles, and overall bioavailability.[21,22]

Encapsulation efficiency, defined as the percentage of active compound successfully incorporated into the NEs, is highly dependent on the hydrophobic properties of the oil, such as polarity, viscosity, saturation, and chain length.[23] Oils with appropriate characteristics can improve drug solubility and retention in the core, maintaining high EE% and optimizing delivery performance.[24,25] Accurate EE% quantification also requires carefully selected purification strategies tailored to the oil-drug interaction,[26] as inappropriate purification can lead to misleading measurements and limit clinical applicability.[27]

Beyond EE%, the oil phase influences the biodistribution, the solubility, the stability, and the cellular uptake of the nanoformulation.[28,29] It also plays a decisive role in enabling co-encapsulation of multiple agents, allowing for synergistic drug combinations that can enhance therapeutic outcomes.[30,31] Moreover, formulation components may interact with biological pathways, potentially leading to either beneficial or unintended effects.[32,33]

Given these multifaceted roles, the rational design of lipid-based nanocarriers is essential to advancing nanomedicine. For example, nanomedicines derived from natural products have demonstrated enhanced targeting, reduced toxicity, and greater therapeutic efficacy.[35] Likewise, fatty alcohol-modified prodrug nanoassemblies have shown that longer alkyl chains improve nanostructure stability and extend circulation time, although this may lead to slower drug release.[34]

Despite these advances, comprehensive studies that systematically investigate how oil composition affects NE stability, drug loading, and therapeutic performance remain limited. Gaining such insights is crucial for optimizing NE systems and accelerating their clinical translation.

Verteporfin (VP) is a second-generation photosensitizer approved by the FDA for use in photodynamic therapy (PDT).[36] Activated by near-infrared light (689 nm),[37] it enables deeper tissue penetration than earlier photosensitizers, making it particularly suitable for treating tumors in less accessible locations. However, its pronounced hydrophobicity, low bioavailability, and off-target accumulation limit its clinical efficacy and necessitate encapsulation strategies to improve tumor specificity and therapeutic efficacy.

In this study, we formulated VP-loaded NEs using two distinct oil cores: oleic acid (OA) and Miglyol (MG). OA, a monounsaturated fatty acid, is amphiphilic and integrates into cellular membranes, enhancing membrane fluidity and potentially facilitating intracellular delivery. Its endogenous origin and involvement in both lipid metabolism and oxidative stress make it especially attractive for targeting cancer-specific lipid vulnerabilities.[38,39] In contrast, MG is a chemically stable medium-chain triglyceride derived from caprylic and capric acids, offering excellent solubilizing capacity, low viscosity, and a well-established safety profile.[40]

Although VP has been previously incorporated into various lipid-based systems, the effect of oil core composition on encapsulation efficiency, stability, cytotoxicity, and photodynamic performance has not been systematically studied.[41–43]

By directly comparing OA- and MG-based VP-loaded NEs, this study provides new insights to guide the rational design of safer and more effective nanoemulsion platforms for PDT. Our findings demonstrate that the oil phase plays a central role in determining both the physicochemical characteristics and therapeutic behavior of these nanocarriers.

2. Materials and methods

2.1. Materials

2.1.1. Reagents and solvents. Oleic acid ≥ 99% (GC), cholesterol ≥ 99%, dimethyl sulfoxide (DMSO), verteporfin (VP) ≥ 94% (HPLC), phosphotungstic acid hydrate, and thiazolyl blue tetrazolium bromide, 98% were purchased from Sigma-Aldrich® (Darmstadt, Germany). Miglyol® 812 was purchased from CREMER OLEO GmbH & Co. KG (Deutschland, Germany). Ethanol (absolute) was purchased from Scharlab, S.L. (Barcelona, Spain). Lipoid® S100 PC (18 : 0/18 : 1) from soybean (94%) was a gift from Lipoid GmbH (Ludwigshafen, Germany). McCoy Medium was purchased from Gibco® (Grand Island, USA). MQ-water was purified using a Millipore Direct-Q 3 system with a UV detector. Tissue culture dishes (100 mm) were provided by VWR International, LLC Avantor® (Barcelona, Spain). 96-well plates and ultra-low-attachment 24-well plates were purchased from Corning Inc. (NY, USA). Syringe filters were purchased from Labbox (Barcelona, Spain).

2.1.2. Cell cultures. High-serous ovarian cancer carcinoma SKOV-3 was purchased from Merck-Sigma-Aldrich® (Darmstadt, Germany) and cultured in McCoy's 5A media. The cell culture medium was supplemented with 10% fetal bovine serum and 1% penicillin–streptomycin. Cells were cultured at 37 °C in a humidified atmosphere containing 5% CO_2. At 85% confluence, cells were harvested using 0.05% Trypsin–EDTA (5 min, 37 °C).

2.2. Synthesis and encapsulation procedures of pure NEs and VP-loaded NEs

2.2.1. Formulation of NEs. NEs were prepared at a 1 mL scale by the low-energy self-emulsification oil-in-water method, following the publication of Carmona-Ule *et al.*[33] Briefly, the stock solution of the lipids phosphatidylcholine (PC) (10 mg mL^{-1}), cholesterol (CH) (10 mg mL^{-1}), and the oils, oleic acid (OA) and miglyol 812 (MG) (100 mg mL^{-1}) were prepared in ethanol and mixed in a ratio of 1 : 1 : 10. Then, the organic phase (100 μL) was quickly injected into deionized water (900

μL), under magnetic stirring at room temperature. After 15 minutes, stirring was stopped and NEs were obtained. The formulations were stored at 4 °C.

Fluorescent NEs were prepared using TopFluor® PC (1-palmitoyl-2-(dipyrrometheneborondifluoride undecanoyl-*sn*-glycero-3-phosphocholine)), which was added to the formulation in a proportion of 4 : 1000 v/v.

2.2.2. Formulation of VP-NEs. Verteporfin nanoemulsions (VP-NEs) were prepared by adding the drug into the organic phase. Firstly, the VP stock solution was prepared by dissolving 0.15 mg of the drug in a mixture of ethanol : DMSO (77 : 23%) at a final concentration of 0.15 mg mL^{-1}. After that, different VP-NEs were prepared depending on the required theoretical VP concentration (from 3 to 1.2 × 10^{-4} mg mL^{-1}) by adding the corresponding volume (from 2 to 8 μL, respectively) of the VP stock to the organic phase. Then, the organic phase was injected into the aqueous phase, under magnetic stirring at room temperature.

After 15 minutes, stirring was stopped, and VP-NEs were obtained. The formulations were stored at 4 °C.

2.2.3. Characterization of NEs

2.2.3.1. Dynamic light scattering (DLS). The NEs were characterized by measuring their hydrodynamic diameter (size) and polydispersity index (PDI) using Malvern® Zetasizer® (Nano ZS90, Malvern). The zeta potential (*Z*-potential) was determined using zeta cells (Malvern). All measurements were taken using a 1 : 10 v/v dilution ratio in Milli-Q water.

2.2.3.2. Nanoparticle tracking analysis (NTA). The number of nanoparticles per mL of each type of NEs sample was assessed by using a Nanosight instrument (Malvern). All measurements were taken using a 1 : 100 v/v dilution ratio in water.

2.2.3.3. Transmission electron microscopy (TEM). TEM images were obtained on a Philips CM20 microscope at an acceleration voltage of 100 kV. For the preparation of the samples, NEs were previously stained with phosphotungstic acid (PTA, 2%) in a dilution of Milli-Q water : phosphotungstic acid (1 : 10); then a drop of the dispersion was placed on a Cu grid, letting the liquid evaporate at room temperature.

2.2.3.4 Optical characterization. Absorbance spectrum of verteporfin was recorded using a Jasco V-730 spectrophotometer (Jasco, Spain) equipped with a Xenon lamp as the excitation source, operating within the spectral range of 300–750 nm (Fig. 1). All spectrophotometric analyses were conducted using a quartz cuvette with a 1 cm optical path length. Importantly, in these measurements, to eliminate noise from the organic phase, a blank sample consisting of 100 μL of empty NEs mixed with 800 μL of ethanol was used in all measurements.

Photoluminescence (PL) spectra of verteporfin were obtained using a Cary Eclipse spectrometer with a Xenon lamp as light excitation source and working in the spectral range of 190–1100 nm. The control VP solution in EtOH had a concentration of 5.7 × 10^{-5} mg mL^{-1} (SI1). All measurements on the solutions were performed using a quartz Suprasil cuvette with an optical path of 1 cm.

In both measurements, NEs-based on oleic acid and miglyol oils were prepared according to Sections 2.2.1 and 2.2.2.

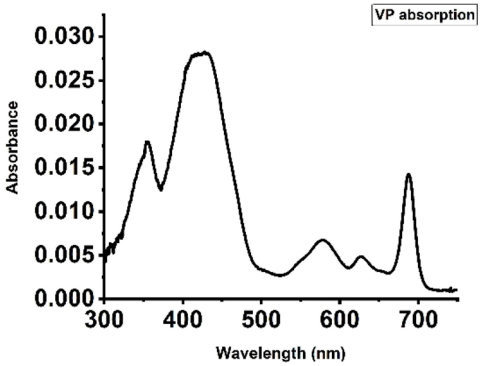

Fig. 1 Verteporfin absorption spectrum showing a maximum absorbance peak at 425 nm.

2.2.4. Encapsulation efficiency of VP. The concentration of VP loaded into NEs was determined after purification. VP measurements were performed using spectrophotometric measurements (see Section 2.2.3.4), and the concentration was calculated based on a standard calibration curve. To generate the calibration curve, 100 μL of VP solutions at known concentrations (ranging from 0.1 to 1 × 10^{-3} mg mL^{-1}) were mixed with 800 μL of ethanol. The calibration curve was constructed by measuring the absorbance at 425 nm, the maximum absorbance peak of VP, and plotting it against VP concentration (Fig. 2A). The experimental VP concentration after VP-NEs purification was then determined by measuring the absorbance at 425 nm and applying the previously established equation. Finally, the encapsulation efficiency (EE%) was calculated by comparing the experimental VP concentration with the theoretical concentration (Fig. 2B):

$$\mathrm{EE}(\%) = \frac{C_t - C_e}{C_t} \times 100$$

where C_t is the theoretical VP concentration in unfiltered VP-NEs and C_e is the experimental drug concentration in the filtered VP-NEs.

2.2.5. VP-NEs purification

2.2.5.1. Amicon100K ultra centrifugal devices. VP-NEs were placed in the filtration chamber, and the centrifuge tubes were placed into the (Eppendorf 5804 R) centrifuge at different speeds and times (SI2). After centrifugation, the NEs retained in the filtration chamber were resuspended in water, while the aqueous phase containing the free VP was collected for concentration quantification.

2.2.5.2. High-speed centrifugation. VP-NEs were placed in tubes and centrifuged at 14 000 rpm for 8 hours at room temperature. The obtained creamy upper part was isolated by removing the water undernatant with the use of a needle.

2.2.5.3. Syringe filters. VP-NEs were passed through hydrophilic PES (polyethersulfone) and hydrophobic PTFE (polytetrafluoroethylene) membranes with 0.22 μm diameters. Then, C_e from the obtained filtered VP-NEs was measured using spectrophotometry.

2.2.6. Stability studies. The different VP-NEs (VP-OA-NEs and VP-MG-NEs) with VP concentrations between 2 and 4 ×

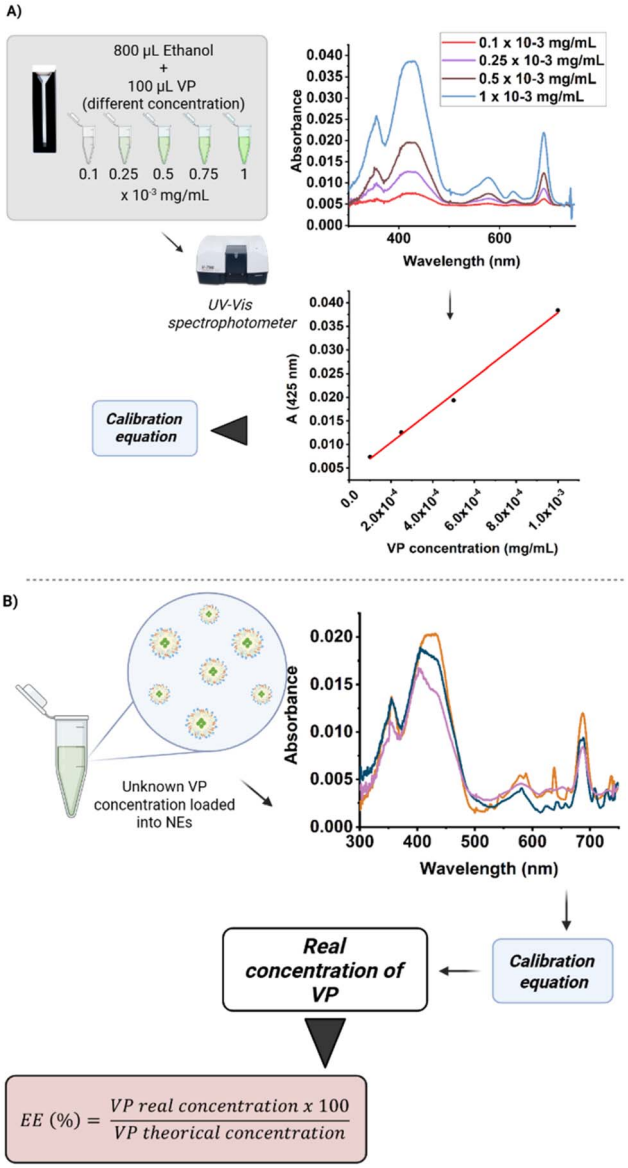

Fig. 2 Scheme (A) illustrates the applied process to generate the calibration curve, (B) spectra for 0.03 (blue), 0.04 (purple), and 0.05 (orange) mg per mL VP loaded into NEs, used to calculate the EE% of VP-loaded NEs.

10^{-4} mg mL^{-1} (C_e) were exposed to three environmental conditions: light and room temperature (RT), RT with protection from light, and storage at −4 °C. For each condition, the VP absorption spectrum, particle size, PDI, and *Z*-potential were measured at three time points: the same day, one week later, and three weeks after their formulation.

2.2.7. Cellular uptake assays

2.2.7.1 Fluoresce microscopy. SKOV3 cells were seeded at a final concentration of 40 000 cells per mL in 0.5 mL per well on Millicell® EZ Slide 8-well glass chambers. The cells were allowed to attach overnight at 37 °C in a 5% CO_2 atmosphere within an incubator. After 24 hours, the cells were treated with NEs, 0.18 × 10^{-4} mg per mL VP-OA-NEs and 1.2 × 10^{-4} mg per mL VP-MG-NEs for 24 hours before imaging. Following treatment, the cells were harvested, washed, and fixed in 4% cold paraformaldehyde for 15 minutes at room temperature. The samples were then washed three times with PBS, and 4′,6-diamidino-2-phenylindole (DAPI) was added for nucleus staining.

The stained samples were then placed under the fluorescence microscope (Leica DMi8 automated microscope, Leica Microsystems) for imaging. A 20× objective was used to capture the 24-hour images. For tracking, fluorescent NEs (TopFluor®) were used in these assays, which allowed for the visualization and tracking of the NEs within the cells. The excitation and emission wavelengths for DAPI staining were 359 nm and 461 nm, respectively. The fluorescence of TopFluor® was visualized using excitation at 485 nm and emission at 512 nm. These settings enabled the precise tracking of nanoemulsions alongside cellular structures.

2.2.7.2 Flow cytometry. SKOV3 cells were seeded in p60-plates at a final concentration of 0.8 × 10^6 cells per plate supplemented with 3 mL per plate of culture medium, and they were allowed to attach overnight at 37 °C in a 5% CO_2 atmosphere within an incubator. After 24 h, culture media was replaced with new media containing fluorescent NEs and VP-NEs (0.18 × 10^{-4} mg mL^{-1}). These were incubated for 24 h and then, the cells were harvested and washed with PBS to remove non-internalized NEs. The internalization of NEs was assessed by using a Cytek Northern Lights flow cytometer. Laser excitation and emission bandpass wavelengths were 488 nm and 530 ± 15 nm (FL1 channel), respectively. The results were reported as the median of the distribution of cell fluorescence intensity obtained by analyzing 10 000 events and were plotted by using the free online software Floreada (Floreada.io).

2.2.8. Viability assays. SKOV-3 cells were seeded in 96-well culture plates at a final concentration of 6000 cells per well supplemented with 100 µL per well of culture medium, and they were allowed to adhere overnight at 37 °C in a 5% CO_2 atmosphere inside an incubator. After 24 hours, the medium was replaced with media containing NEs, VP-NEs, and free VP at different concentrations (calculated by spectrophotometry as previously described): 0.5–2 × 10^{-4} mg mL^{-1} for VP-MG-NEs, 0.1–0.2 × 10^{-4} mg mL^{-1} for VP-OA-NEs, and 0.2–1.5 × 10^{-4} mg mL^{-1} for free VP. Triton was used as a positive control of cell death. The cells were treated for 24 hours, after which the media were removed and replaced with media containing 3-(4, 5-dimethylthiazol-2-yl)-2, 5-diphenyltetrazolium bromide (MTT) at a concentration of 0.5 mg mL^{-1}. Then, the medium was removed, and the formed formazan crystals were dissolved in 100 µL of DMSO. After the dissolution of the salts, the absorbance of the wells was measured using a multiple plate reader (Biotek, UK) at 540 nm. The cell viability was calculated from the relative absorbance of control cells at 540 nm and expressed as a percentage of 100% live cells. Three independent repeats were performed for all conditions.

2.2.9. Photodynamic activity of VP, VP-OA-NEs and VP-MG-NEs. SKOV3 cells were seeded in three 96-well culture plates on each experiment at a final concentration of 6000 cells per well supplemented with 100 µL per well of culture medium, and they were allowed to adhere overnight at 37 °C in a 5% CO_2

atmosphere inside an incubator. After 24 h, cells were incubated with VP in three different forms: encapsulated into OA-NEs (VP-OA-NEs), into MG-NEs (VP-MG-NEs) and its free form (VP). After 24 h, two 96-well plates were put under two different intensities (1.0 and 3.3 mW cm^{-2}) of near infrared light (NIR) exposure by using a lamp with a 6 W bulb emitting at 670 nm (Solux®) for 15 min. The third 96-well plate was used as a control of no light by placing it next to the lamp, covered with aluminium paper, for the same time (15 min) outside the incubator. Then, viability assays were performed.

2.2.10. Statistical analysis. Statistical significance was assessed using one-way ANOVA followed by Dunnett's or Tukey's multiple comparisons test for single-factor analyses, after confirming normality. For two-factor analyses, two-way ANOVA followed by Sidak's multiple comparisons test was applied. All statistical analyses were performed using GraphPad Prism 8. Less than 0.05 for *p*-values were considered statistically significant.

3. Results and discussion

3.1. Formulation and characterization of verteporfin-loaded nanoemulsions

To investigate the influence of NE components on their performance, we adopted a strategy involving two distinct formulations. These include verteporfin-loaded oleic acid nanoemulsions (VP-OA-NEs) and verteporfin-loaded miglyol nanoemulsions (VP-MG-NEs).

The formulation methodology selected was the oil-in-water (O/W) method previously reported by our group.[33] The organic phase is based on the lipids phosphatidylcholine (PC) and cholesterol (CH), which are key structural components of cell membranes. PC is the major phospholipid in eukaryotic membranes, comprising 40–60% of the lipid bilayer, and plays a crucial role in maintaining membrane fluidity and integrity.[44] Additionally, CH modulates membrane stability and permeability, contributing to the membrane structure.[45] Due to their natural presence in cell membranes, both PC and CH are highly biocompatible and enhance cellular uptake.[46] Oleic acid (OA) and Miglyol® 812 (MG) were chosen as the core components for NEs formulations due to their distinct chemical structures and complementary properties such as biocompatibility, which make them ideal for encapsulating hydrophobic drugs.[47,48]

Verteporfin was selected as the encapsulated drug because it is FDA-approved for photodynamic therapy (PDT) in age-related macular degeneration,[49] simplifying its adaptation for cancer treatments. Its ability to absorb both visible light (~400 nm) and near-infrared (NIR) light (650–690 nm) (Fig. 1 and SI1) allows flexible use: (a) visible light targets surface-level tissues, (b) NIR penetrates deeper to treat tumors buried under skin or organs. Interestingly, due to its characteristic dark green, opaque color, VP can be easily detected by eye when present at high concentrations.[50]

The preparation process of VP-NEs involved dissolving VP at 3×10^{-4} mg mL^{-1} (as testing concentration) in the organic phase containing the selected oil. Characterization by DLS of the formulated NEs revealed that both types exhibited a particle size between 120 and 150 nm, a negative surface charge, and a polydispersity index (PDI) below 0.3. Moreover, around 1.2 and 1.64×10^{11} nanoparticles per mL were produced on the VP-OA-NEs and VP-MG-NEs samples, respectively (Fig. 3A). The similarity in size, charge and number of particles between both formulations proves the reproducibility of the employed methodology. The particle size measurements obtained by dynamic light scattering (DLS) (Fig. 3A) revealed larger sizes for both VP-OA-NEs and VP-MG-NEs compared to those observed in the transmission electron microscopy (TEM) images (Fig. 3B). This difference is expected, as DLS measures the hydrodynamic diameter, which includes the solvation layer around particles, whereas TEM reflects the actual physical size in the dry state. A similar trend was observed for the empty OA-NEs and MG-NEs (SI3), confirming that the discrepancy is inherent to the measurement techniques rather than the payload. These findings are consistent with previous reports comparing DLS and TEM measurements in lipid-based nanoparticles.[51]

3.1.1. Impact of purification strategy on the isolation of verteporfin-loaded nanoemulsions. Once VP-NEs were formulated, a purification step was performed to separate free VP from its encapsulated form. This step is critical to remove the unencapsulated VP, as this detrimentally impacts the accuracy of dosing and therapeutic efficacy of the NEs. Three different purification techniques were tested: (A) Amicon®ultra-centrifugal filters, (B) ultracentrifugation, and (C) syringe filters.

3.1.1.1 Amicon® ultra-centrifugal filters. Amicon® filters were selected because they are widely used for molecular weight-based filtration due to their high efficiency. These devices utilize ultrafiltration to retain larger particles, such as NEs, while allowing smaller molecules, like free VP, to pass through. Our previous experience successfully separating peptide-functionalized NEs from free peptide further supported

A) Physico-chemical characteristics

Parameters	VP-OA-NEs VP (3×10^{-4} mg/mL)	VP-MG-NEs VP (3×10^{-4} mg/mL)
Dynamic Light Scattering (DLS)		
Size (nm)	144 ± 2	120 ± 6
PDI	0.11 ± 0.05	0.10 ± 0.01
Charge (mV)	-28.00 ± 8.55	-28.70 ± 0.96
Nanoparticle Tracking Analysis (NTA)		
Nº nanoparticles (nps/mL)	1.2×10^{11}	1.6×10^{11}

B) Transmission Electron Microscopy (TEM)

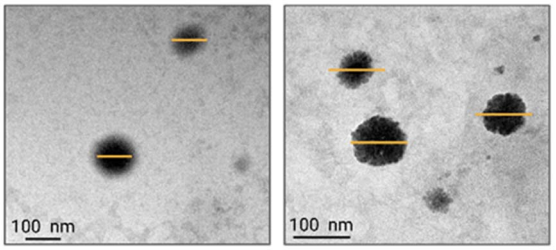

Fig. 3 (A) Physico-chemical characterization of VP-OA-NEs and VP-MG-NEs. (B) Transmission Electron Microscopy (TEM) analysis of VP-OA-NEs and VP-MG-NEs.

the use of this method for separating free VP from encapsulated VP in our VP-NEs.[52] To optimize the separation process, various centrifugation speeds and durations were tested (SI2). The separation efficiency was assessed by evaluating the integrity of the NEs, focusing on their size and PDI to ensure stability and uniformity after purification.

Our results showed that Amicon® filters were unsuitable for separating VP-OA-NEs, as significant destabilization occurred after filtration. Initially, the NEs exhibited a size of approximately 140 nm with a PDI of 0.1–0.2; however, after filtration, the size increased dramatically, exceeding 1000 nm, with a PDI of 1 (SI2).

This destabilization aligns with previous studies showing that high centrifugal speeds using Amicon® filters can induce nanoparticle aggregation, compromising stability and physical characteristics.[53] These findings highlight the limitations of Amicon® filters in applications requiring precise control over nanoparticle size and stability.[54] In our case, the need for high centrifugal speeds arose from the retention of VP within the filter membrane, due to its hydrophobic nature and strong affinity for the filter material. This hindered complete separation, as also reported in previous studies.[55] As a result, free VP was observed floating on the surface upon recovery, further underscoring the inadequacy of this purifying approach for hydrophobic molecules like VP.

3.1.1.2 Ultracentrifugation. The methodology is based on the separation of two phases using differences in density between free VP and VP-OA-NEs. Various centrifugation times and speeds were assessed, but 8 hours at the maximum speed of 14 000 rpm was required to achieve two distinct phases: an upper creamy phase containing the VP-OA-NEs and a clear bottom phase with VP droplets, which appeared green due to the optical properties of VP. Applying this methodology, VP-OA-NEs did not show an increase in size or PDI, indicating that the NEs remained stable throughout the process (SI2). However, it was observed that the purification was not entirely successful. Indeed, after separation, small green droplets, indicative of free VP, were still visible in the supernatant where the NEs were suspended. This suggests that while centrifugation helped to separate the phases partially, the retention of free VP in the supernatant limited the overall effectiveness of this method for purifying the VP-OA-NEs.

3.1.1.3 Syringe filters. Syringe filters are used to remove particles from a liquid sample before analysis or injection. We used polyethersulfone (PES) syringe filters, which were shown to be effective in separating free VP from encapsulated VP in OA-NEs while maintaining sterility. The hydrophilic PES filters allowed the VP-OA-NEs to pass through while retaining the hydrophobic free VP. After centrifugation, the NEs retained their properties, with only a slight decrease in size and an improvement in PDI. The VP spectrum remained unchanged, confirming that the encapsulated VP was successfully separated from the free VP (Fig. 4).

The previously mentioned minor decrease in particle size is likely due to mechanical stress during filtration, which may have disaggregated larger NEs. However, the PDI showed no significant change, indicating that the size distribution

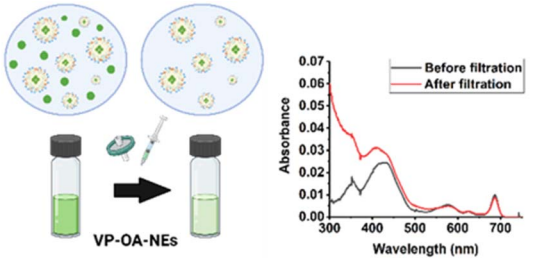

	Before centrifugation		After centrifugation	
	Size (nm)	PDI	Size (nm)	PDI
VP-OA-NEs	180 ± 9	0.24 ± 0.05	147 ± 7	0.16 ± 0.06

Fig. 4 At the top, a scheme showing the use of PES filters and the spectrum of VP-OA-NEs before and after filtration. At the bottom, data showing the size and PDI of VP-OA-NEs before and after centrifugation.

remained stable. Additionally, Nanoparticle Tracking Analysis (NTA) showed minimal variation in particle number after filtration (SI8), suggesting that the filtration removed larger NEs without compromising the stability and the integrity of the formulations.

Based on these results, it is evident that the effectiveness of the methodology used to separate VP-NEs from free VP is highly dependent on the nature of the separation technique and the physicochemical properties of the drug to be encapsulated. Our findings highlight that for hydrophobic molecules like VP, purification challenges are primarily driven by the affinity of the drug for the filter material, rather than the composition of the oil phase. Since the drug remains unchanged across different nanoemulsion formulations, we applied the same purification strategy to VP-MG-NEs.

3.2. Encapsulation efficiency of OA-NEs and MG-NEs and strategies for improvement

Once the purification methodology for VP-loaded NEs was selected, the encapsulation efficiency (EE%) was determined using a theoretical VP concentration of 3×10^{-4} mg mL^{-1}. The amount of encapsulated VP was quantified directly by UV-Vis absorbance measurements, using a previously constructed calibration curve (Fig. 2, Section 2.2.4). The concentration of VP encapsulated in the NEs was calculated, giving an average EE% of 35.59 ± 5.36% for VP-OA-NEs and 34.16 ± 5.20% for VP-MG-NEs (SI4).

To increase the EE%, we modified: (a) the experimental procedure by modulating the injection method and (b) the ratio of the organic phase during the formulation process, as explained in the following scheme (Scheme 1).

3.2.1 Effect of the injection method on VP encapsulation efficiency. It is well known that the method used to formulate lipid nanoparticles has a significant impact on EE%,[56] however, there is limited information available regarding the experimental procedures employed. It is worth noticing that in this work, initially, during the formulation process, as explained in paragraph 3.1, the organic phase was injected from above into

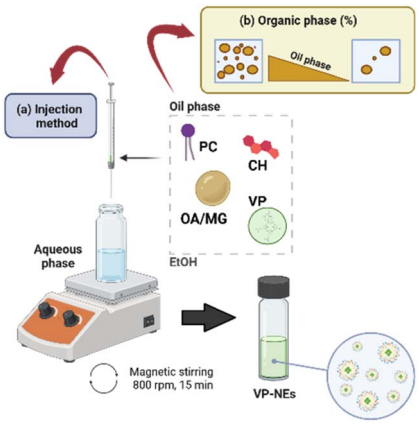

Scheme 1 Schematic representation of the two-step strategy to increase the encapsulation efficiency of verteporfin in nanoemulsions: (a) optimization of the injection method, and (b) adjustment of the organic phase proportion.

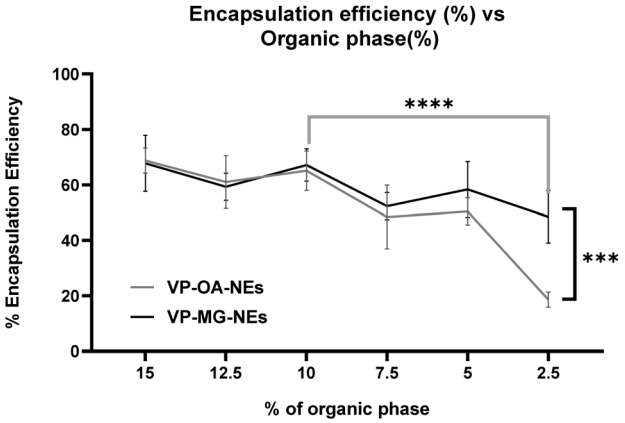

Fig. 5 Encapsulation efficiency VP as a function of the organic phase percentage in VP-OA-NEs (grey) and VP-MG-NEs (black). All formulations were prepared with a fixed VP concentration of 0.3×10^{-4} mg mL^{-1}. Measurements were done in triplicate. Differences in encapsulation efficiency within each formulation at different organic phase concentrations were assessed using one-way ANOVA. ***$p < 0.0005$, ****$p < 0.0001$. Differences in VP encapsulation between the two formulations at each concentration were assessed using two-way ANOVA. ***$p < 0.0005$, ****$p < 0.0001$.

the aqueous phase, without contact between the needle and the aqueous phase. However, when the needle is inserted directly into the aqueous phase, the EE% was almost doubled from 35.59 up to 68.55 for VP-OA-NEs and 36.16 up to 71.48 for VP-MG-NEs (SI5).

The differences observed in the EE% results highlight the importance of evaluating all parameters involved in developing a drug delivery system. In this case, the low EE% observed with the first injection method is not attributed to poor nanoparticle formation, but rather to inefficient drug encapsulation. This is likely due to the limited ability of the solvent–lipid interface (organic phase) to diffuse rapidly into the aqueous phase, which affects the incorporation of the drug into the forming nanoparticles, despite successful particle assembly.[57,58] In contrast, the rapid and controlled injection, during the second injection, facilitates better mixing, promoting the formation of smaller droplets and enhancing the encapsulation of hydrophobic molecules like VP within the oil core of the nanoemulsion.

3.2.2 Effect of organic phase proportion on VP encapsulation efficiency in nanoemulsions as a function of the oil core. The second step involved modifying the oil-to-water ratio. The ratio utilized in the standard formulation was 10% of the organic phase to 90% of the aqueous phase.[33] Here, in a way to improve the EE% VP into the oil core, six different organic phase percentages were tested for each type of VP-loaded NEs (OA-VP-NEs and MG-VP-NEs): 10% (the standard), 12.5%, and 15% (above the standard), and 7.5%, 5%, and 2.5% (below the standard). The results are presented in Fig. 5.

As shown in Fig. 5, a decrease in EE% was observed when the organic phase was reduced from 10% to 7.5% for both VP-OA-NEs and VP-MG-NEs. However, this reduction was not statistically significant, indicating that encapsulation efficiency remained relatively stable within this range. A further decrease to 5% led to a slight, non-significant increase in EE%. Notably, when the organic phase was reduced to 2.5%, VP-OA-NEs exhibited a significant drop in EE% to approximately 18% ($p <$ 0.0001), while VP-MG-NEs remained unaffected. Conversely, increasing the organic content to 12.5% and 15% did not yield any significant improvement in VP loading for either formulation. These findings suggest that a 10% oil phase provides an optimal balance, maintaining high encapsulation efficiency without the need for further increases in organic content.

Previous studies have also reported 10% as the optimal proportion of the organic phase to achieve the highest EE% of hydrophobic drug encapsulation. For instance, Hassanzadeh and colleagues observed that the EE% of garlic oil decreased from 92% to 77% as the oil-to-emulsion ratio increased from 10% to 25%. Interestingly, at 5% oil, matching the concentration tested in our study, the EE% was slightly lower than at 10%, consistent with our results.[59] Additionally, it has been reported that increasing the oil percentage (*e.g.*, flaxseed oil) from 10% to 40% results in emulsions with larger droplet sizes and higher viscosity, which negatively affects surface oil content.[60] Similarly, Mazloom and Farhadyar demonstrated that the encapsulation efficiency declined as the concentration of blueberry essential oil increased in nanoemulsion formulations.[61] Therefore, the superior encapsulation efficiency of VP observed at 10% oil content in our formulations aligns well with previous findings reported in the literature.

A remarkably consistent difference between the two formulations was observed at oil phase proportions below 7.5%, where the graph lines diverge and remain separated across this range (Fig. 5). This sustained divergence highlights the fundamental physicochemical differences between OA, and MG. These statistical differences ($p < 0.0005$) play a critical role in the formulation and behavior of NEs, particularly at lower oil contents, where maintaining an appropriate balance between the hydrophobic core and the total formulation volume becomes essential. The consistent performance gap underscores the importance of oil phase composition in determining EE% and overall NE stability.

The fluid core morphology of OA facilitates greater molecular mobility of VP (VP, $\log P = 7.1$), promoting drug leakage when the oil content drops below a critical threshold. Its unsaturated structure decreased packing density and lower core rigidity, compromising encapsulation. Additionally, OA-based systems require higher surfactant concentrations to stabilize the interface, further diluting the effective drug-loading capacity and increasing variability in particle size.[62,63]

In contrast, MG forms more tightly packed, cohesive hydrophobic cores due to its saturated triglyceride structure. This leads to improved structural integrity even at oil contents as low as 5–7%, effectively limiting VP diffusion.[64] As a result, VP-MG-NEs exhibit higher EE%, narrower particle size distribution, and greater resistance to leakage under stress conditions.[65] These characteristics make MG-based formulations particularly advantageous for achieving stable encapsulation performance when operating under reduced oil content constraints.

3.3. Assessment of NE loading capacity and its impact on encapsulation efficiency by increasing theoretical verteporfin concentration as a function of the oil core

Once the optimal physicochemical parameters for maximizing EE% were established, the next step was to evaluate the ability of the NEs to encapsulate higher concentrations of VP. This was achieved by progressively increasing the VP concentration in both oleic acid- and miglyol-based formulations. Subsequently, the actual VP concentration encapsulated and the corresponding EE% were measured for each formulation condition. To ensure the stability of the obtained formulations during loading, their physicochemical properties, including particle size, polydispersity index, and *Z*-potential, were monitored. The results summarized in SI6 show no significant differences in size, polydispersity index, or *Z*-potential, indicating stable physicochemical properties regardless of the VP concentration loaded into OA- and MG-based NEs.

The plotted results show that increasing the theoretical concentration of VP leads to a corresponding rise in the actual encapsulated amount for both VP-OA-NEs and VP-MG-NEs (Fig. 6A). However, VP-OA-NEs exhibit a modest increase in VP loading, from 0.21×10^{-3} mg mL^{-1} to a maximum of 0.36×10^{-3} mg mL^{-1}, even when the theoretical concentration is raised from 0.3×10^{-3} mg mL^{-1} to 1.2×10^{-3} mg mL^{-1} (SI6), suggesting early saturation. In contrast, VP-MG-NEs show a more linear and pronounced increase, reaching 0.88×10^{-3} mg mL^{-1} at the same theoretical concentration (SI6). A statistically significant difference in encapsulated VP was observed between the two formulations at theoretical concentrations above 0.7×10^{-3} mg mL^{-1}, indicating that MG-based NEs can accommodate higher drug loads.

Analysis of encapsulation efficiency (EE%) further supports this observation. In VP-OA-NEs, EE% declines as the theoretical VP concentration increases, reflecting saturation of the oleic acid-based system. This likely results from structural constraints in OA that limit the number of hydrophobic compartments available to incorporate VP. Conversely, VP-MG-NEs maintain a relatively stable EE% between 65–80%, even as VP input increases, enabling greater drug loading. This difference may be attributed to the oil core properties of MG, such as lower polarity, greater fluidity, or favorable molecular packing, which allow more efficient encapsulation.

Importantly, regardless of loading levels, VP retains its characteristic photophysical properties in both NEs systems (SI1). Fluorescence spectra display the typical VP emission band near 700 nm under 425 nm and 652 nm excitation (Fig. 7), with negligible fluorescence from unloaded NEs. This confirms that photodynamic potential of VP is preserved upon encapsulation in both OA- and MG-based NEs.

Several studies have reported significant variations in drug loading efficiency based on the composition of the oil core in NEs.[66] The choice of oil phase is primarily determined by the solubility of the drug, a key factor influencing encapsulation efficiency and stability.[67] Optimization of the oil core is therefore critical for achieving optimal performance in drug delivery applications. Key parameters affecting drug solubility within the oil core include degree of saturation, viscosity, hydrophobicity, and oxidation resistance.[68–70] In our study, MG, a mixture of medium-chain triglycerides predominantly composed of saturated fatty acids such as caprylic acid (C8) and capric acid (C10), is highly hydrophobic due to its saturated triglyceride structure, providing excellent stability. In contrast, OA, a monounsaturated fatty acid with 18 carbon atoms and a double bond at the 9th position, possesses a free carboxyl group, introducing some polarity and making it less hydrophobic than MG. Our data revealed that the higher hydrophobicity and apolarity of MG enhance the EE% of VP in NEs, leading to increased drug loading capacity and improved formulation stability. Thus, MG is a more suitable choice for NEs requiring enhanced drug loading and stability.

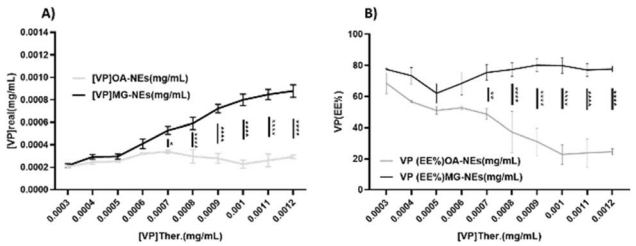

Fig. 6 (A) Comparison of theoretical *vs.* real VP concentrations loaded into OA-NEs (grey) and MG-NEs (black). (B) Encapsulation efficiency (%) of VP in OA-NEs and MG. Measurements were performed in triplicate. Differences in VP encapsulation and EE% within each formulation at different concentrations were assessed using one-way ANOVA. $*p < 0.05$. Differences in VP encapsulation and EE% between the two formulations two-way ANOVA. $*p < 0.05$.

3.4. Study of the stability of VP-loaded OA and MG-NEs under different conditions

Once the VP-loaded NEs were formulated, the stability of both VP and the NEs (loaded with VP), under different storage conditions, was assessed. To evaluate VP stability, changes in its spectrum were monitored at three different theoretical

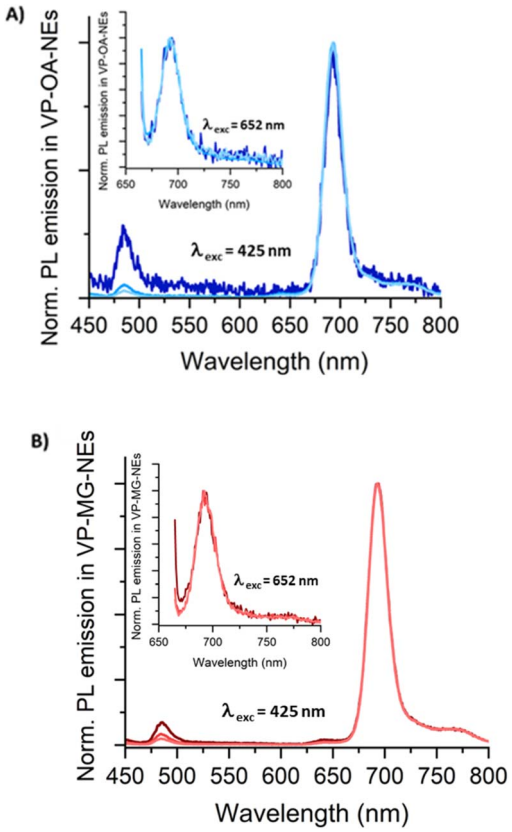

Fig. 7 Photoluminescence spectra of (A) VP-OA-NEs and (B) VP-MG-NEs with increasing VP nominal concentrations at 3×10^{-4}, 4×10^{-4}, and 6×10^{-4} mg mL^{-1} (solid lines from the darkest to the lightest blue (OA) and red (MG) colors, respectively) in EtoH under 425 nm and 652 nm (insets) excitation is presented. All the spectra are normalized to their maxima.

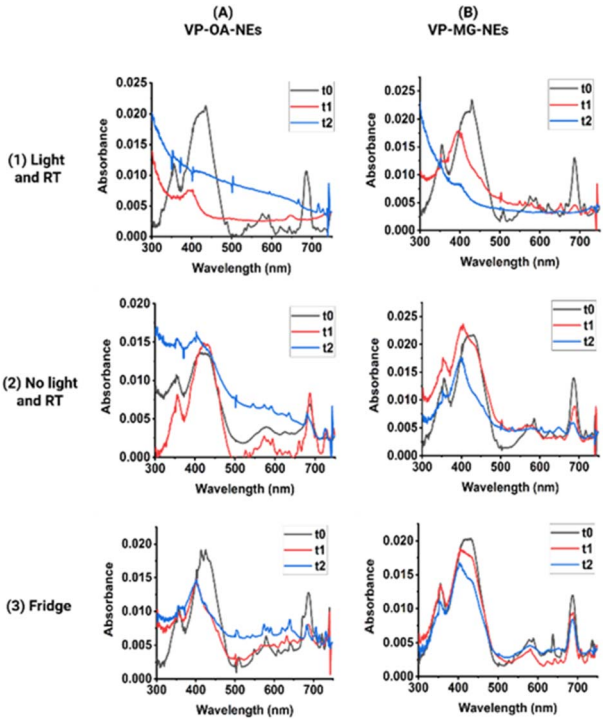

Fig. 8 The graphs display the degradation of the VP absorption spectra for OA-VP-NEs (A) and MG-VP-NEs (B) (4×10^{-4} mg mL^{-1}) under three different conditions: (1) light and room temperature, (2) no light and room temperature, and (3) fridge (−4 °C), each measurement was taken at three different times (t_0; 1 day after preparation, grey), t_1 (1 week after preparation, red) and t_2 (3 weeks after preparation, blue).

concentrations (C_t) (3, 4, and 5 × 10^{-4} mg mL^{-1}) and three different conditions: (1) room temperature under normal light conditions, (2) room temperature in darkness, (3) refrigerated at −4 °C. Additionally, the physicochemical properties of the VP-OA-NEs and VP-MG-NEs, including size, zeta potential, and polydispersity index (PDI), were measured SI7. Comparative graphics showing changes in the VP spectra over time under various storage conditions (C_t: 4×10^{-4} mg mL^{-1}) are shown in Fig. 8, while data for C_t: 3 and 5×10^{-4} mg mL^{-1} are provided in SI7.

The spectra obtained from VP-loaded OA-NEs show degradation of the drug after three weeks (t_2) under all tested conditions. In contrast, the VP spectra from MG-NEs maintained their absorbance signal, except under condition 1 (light and room temperature), where complete degradation also occurred. These results highlight the crucial role of the oil phase in protecting VP from degradation, as well as the significant impact of light exposure in accelerating VP degradation over time. Additionally, storage temperature influenced stability, with VP-NEs stored at 4 °C (assumed to be in the dark) showing less degradation compared to those stored at room temperature. Physicochemical characterization over time revealed only minor differences between each formulation. Notably, both maintained stable PDI and zeta potential values throughout the study, indicating consistent surface charge and particle distribution. However, VP-OA-NEs exhibited a slight increase in particle size over time, particularly at room temperature with light exposure, suggesting some structural instability. In contrast, VP-MG-NEs maintained a consistent particle size, indicating better structural integrity.

The observed increase in particle size for VP-OA-NEs may be attributed to VP degradation under these storage conditions (Fig. 9A and B), which likely destabilizes the NE formulation by altering its chemical structure. Moreover, as previously noted, the presence of a double bond in oleic acid renders it more susceptible to oxidation, further compromising the stability of the NEs. Based on these findings, VP-NEs formulated with a MG core are likely to exhibit greater stability due to their reduced susceptibility to oxidation.

3.5. Qualitative and quantitative analysis of VP-NEs uptake in ovarian cancer cells

The potential internalization of VP-OA-NEs and VP-MG-NEs in SKOV-3 cells was assessed using fluorescence microscopy and flow cytometry.

3.5.1. Qualitative analysis of NEs uptake by fluorescence microscopy. From the fluorescent images shown in Fig. 10, successful internalization of OA-NEs, VP-OA-NEs, MG, and VP-MG-NEs into SKOV-3 cells can be observed. The intracellular

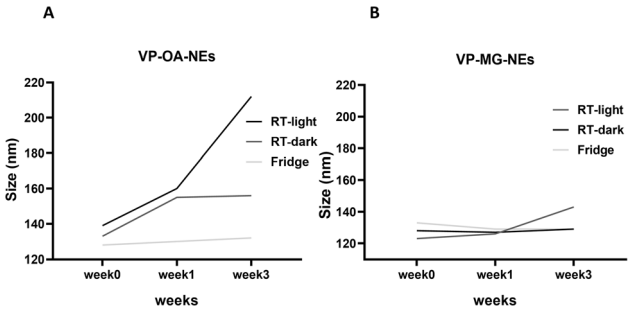

Fig. 9 Changes in particle size of VP-loaded NEs over a 3-week period: (A) VP-OA-NEs and (B) VP-MG-NEs.

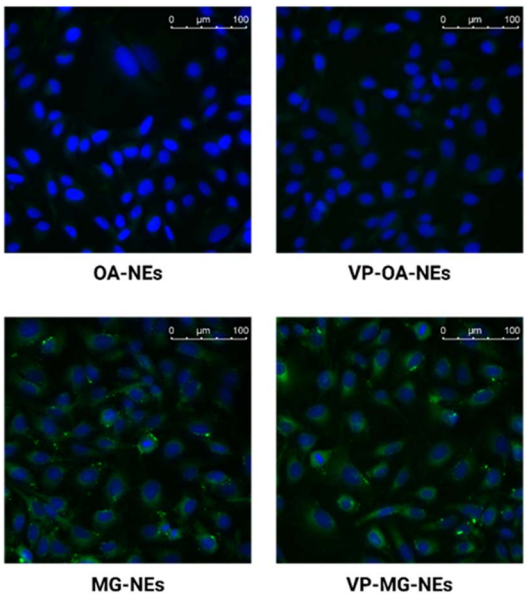

Fig. 10 Fluorescent images of SKOV3 cells treated with NEs and VP-NEs. On the left, cells were incubated with NEs, whereas on the right, they were incubated with VP-NEs (0.18×10^{-4} mg mL^{-1} in VP-OA-NEs and 1.2×10^{-4} mg mL^{-1} in VP-MG-NEs). NEs are visualized in green while cell nuclei in blue.

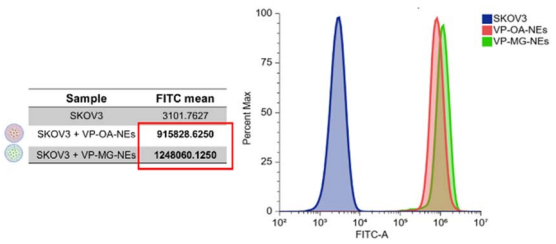

Fig. 11 On the right, FITC fluorescence histograms showing the uptake of VP-OA-NEs (red) and VP-MG-NEs (green) in SKOV-3 cells compared to untreated control cells (blue). A clear fluorescence shift confirms the higher cellular internalization of VP-MG-NEs compared to VP-OA-NEs. On the left, quantification of FITC mean fluorescence intensity (MFI) in SKOV-3 cells treated with VP-OA-NEs or VP-MG-NEs nanoemulsions were labelled with TopFluor® PC, allowing detection *via* FITC-A channel.

fluorescence signal is predominantly localized in the cytoplasm, indicating efficient cellular uptake and reinforcing the potential of these NEs as effective delivery systems for VP. Notably, the MG-based formulations display a more intense fluorescence signal than the OA-based counterparts. This is likely due to both a higher internalization efficiency (3.5.2) and the use of a higher concentration of MG-NEs in the experiment. The lower intrinsic toxicity of MG formulations (3.6) allowed us to apply a greater amount of NEs without compromising cell viability, thereby enabling clearer visualization under fluorescence microscopy.

3.5.2 Qualitative analysis of nanoemulsion uptake by flow cytometry. The internalization of VP-OA-NEs and VP-MG-NEs in SKOV-3 cells was assessed by using flow cytometry. After incubation with the VP-NEs, cells were harvested and analyzed to quantify fluorescence intensity, which reflects the extent of NEs uptake.

Flow cytometry analysis confirmed the internalization of both VP-loaded-NEs by SKOV-3 ovarian cancer cells. However, a noticeable rightward shift in the FITC fluorescence peak, along with increased mean fluorescence intensity (MFI), was observed in cells treated with VP-MG-NEs compared to VP-OA-NEs (Fig. 11). The use of TopFluor® PC as a membrane-inserted fluorescent tracer allowed us to track the surface-associated NEs, reinforcing that the observed signal shift corresponds to actual uptake and not just surface binding.

This indicates a significantly higher cellular uptake of VP-MG-NEs. The enhanced internalization is likely influenced by the physicochemical properties of the oil core: Miglyol 812, produces NEs with lower viscosity, more compact droplet size, and greater colloidal stability, which are favorable characteristics for efficient endocytosis by cancer cells.[71] In contrast, oleic acid, due its long-chain unsaturated fatty acid, may affect membrane, particle interactions differently due to its conformational flexibility and surface activity.

These findings are consistent with prior studies showing that nanocarrier uptake can be modulated by lipid composition, surface fluidity, and particle elasticity, which together influence membrane wrapping and internalization dynamics.[72] This highlights the critical importance of formulation parameters, such as oil phase selection, in optimizing nanomedicine design to enhance drug delivery and improve the therapeutic index. By promoting higher cellular uptake, increased intracellular accumulation of VP can significantly influence therapeutic outcomes, as photodynamic efficacy strongly depends on both intracellular drug availability and its subcellular localization.

3.6. Comparative cytotoxicity of OA and MG based NEs and their verteporfin-loaded versions in ovarian cancer cells

The initial step involved evaluating the intrinsic cytotoxicity of the NEs in the absence of VP. To this end, increasing concentrations of OA-NEs and MG-NEs, relative to the number of nanoparticles per milliliter (SI8), were added to SKOV-3 cells, and cell viability was assessed. As shown in Fig. 12, OA-NEs induced notable toxicity at 6.1×10^{9} particles per mL, while MG-NEs were well tolerated even at concentrations as high as

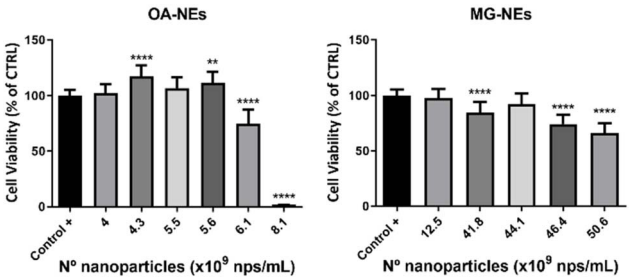

Fig. 12 Cell viability of SKOV-3 ovarian cancer cells following treatment with increasing concentrations of (OA-NEs, left) and (MG-NEs, right). Viability is expressed relative to untreated control cells (set at 100%). Data are presented as a function of no. particle ($n = 3$). Statistical significance was assessed using two-way ANOVA followed by Dunnett's post hoc test. $^{**}p < 0.005$; $^{***}p < 0.0001$.

441×10^9 particles per mL. This observation aligns with previous studies showing that unsaturated fatty acids such as OA can disrupt membrane integrity, induce lipid peroxidation, and activate stress pathways in cancer cells by modulating membrane fluidity and promoting oxidative stress.[73–75] Mechanistically, the monounsaturated structure of OA may facilitate stronger interactions with cellular membranes and potentially alter lipid raft composition, sensitizing cells to damage even in the absence of an active drug. In contrast, MG-based NEs exhibited significantly lower cytotoxicity, which can be attributed to the saturated, chemically inert nature of Miglyol® 812, a medium-chain triglyceride recognized for its biocompatibility and minimal interaction with cellular membranes.[76,77] Contrasting OA, MG lacks unsaturation and therefore does not disturb membrane fluidity or induce oxidative stress, resulting in a more inert carrier that preserves cellular viability at higher concentrations. This enhanced stability and reduced biological activity make MG a favorable oil phase for formulations where minimal carrier-associated cytotoxicity is desired.

To evaluate the cytotoxic potential of the complete formulations, VP-OA-NEs and VP-MG-NEs were tested in SKOV-3 cell line, using empty OA-NEs and MG-NEs as controls. Free VP displayed an IC_{50} of 0.25×10^{-4} mg mL^{-1}, while VP-OA-NEs exhibited a lower IC_{50} of 0.2×10^{-4} mg mL^{-1}, suggesting that encapsulation in OA-based nanoemulsions lightly enhances the cytotoxic effect of VP. This enhancement may be attributed to the bioactive nature of OA, as previously observed in our control experiments, where OA-NEs showed higher intrinsic cytotoxicity than MG-NEs. In agreement with this low cytotoxicity of MG-NEs, data showed how VP-MG-NEs exhibited minimal cytotoxicity across all tested concentrations (Fig. 13), with only a slight reduction in viability at the highest dose (1.25×10^{-4} mg mL^{-1}). This low pre-activation toxicity proves again, the limited interaction of Miglyol® 812 with biological membranes. These results also suggest that MG-based formulations offer a protective carrier environment for VP, preventing off-target effects prior the activation of the VP with the specific light.

Additionally, in SKOV-3 cells, VP-OA-NEs triggered a sharp loss of viability between 0.18 and 0.2×10^{-4} mg mL^{-1}, comparable to the Triton X-100 control, indicating a narrow

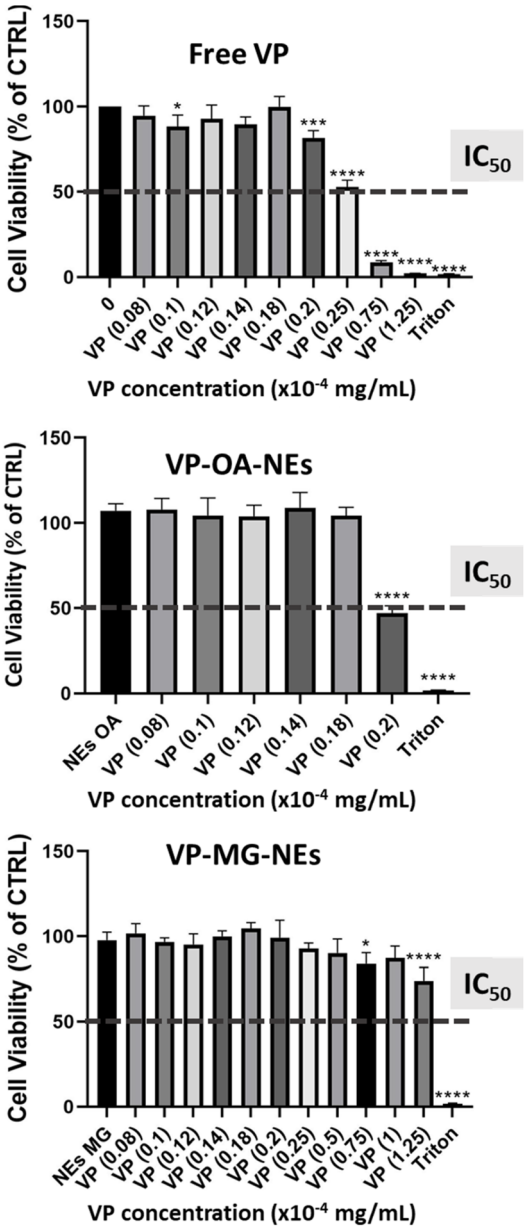

Fig. 13 Cell viability of SKOV-3 cells following treatment with increasing concentrations of VP-loaded nanoemulsions: VP-OA-NEs and VP-MG-NEs. Corresponding blank nanoemulsions (OA-NEs and MG-NEs) were included as controls and administered at volumes equivalent to those used to achieve the highest VP concentration. Viability is expressed relative to untreated control cells (set at 100%). Differences between free VP and VP-loaded nanoemulsions were analyzed using two-way ANOVA. $^{**}p < 0.005$; $^{***}p < 0.0005$; $^{***}p < 0.0001$. Data represent mean ± SD ($n = 3$).

therapeutic window. These findings underscore the importance of evaluating each nanoemulsion component individually, particularly the oil core, as it significantly influences both formulation stability and biological activity. The marked differences between VP-MG-NEs and the other groups (free VP and VP-OA-NEs) highlight the critical role of the oil phase in modulating cytotoxicity and guiding therapeutic applications.

Previous studies have shown that oleic acid-based formulations, including ozonized nanoemulsions (OZNEs), can exert anticancer effects through oxidative stress and membrane destabilization mechanisms.[78] OA has also been linked to enhanced endocytosis, pro-apoptotic signaling, and modulation of intracellular trafficking.[79] Importantly, OA-based nanocarriers have shown efficacy even in non-photoactivated contexts: enzyme-responsive OA nanocapsules have enabled efficient intracellular payload release, and Pt(II)-loaded OA-NEs achieved effective tumor targeting and therapeutic benefit *in vivo*.[80] These data support the use of OA-containing nanoemulsions in light-independent anticancer strategies where baseline cytotoxicity is advantageous.

In contrast, VP-MG-NEs demonstrated negligible cytotoxicity in the absence of light, consistent with the established biocompatibility of Miglyol® 812-based systems.[81,82] This low background toxicity is particularly favorable for photodynamic therapy, which relies on light-triggered activation to ensure therapeutic selectivity. MG-NEs have previously been used in biomedical applications such as site-specific drug delivery and diagnostic imaging, valued for their excellent tolerability and stability in biological environments.[83] However, to our knowledge, no prior studies have emphasized their potential to shield cells from premature drug-induced cytotoxicity. Our findings suggest that MG may not only serve as a safe carrier but also facilitate a more controlled activation of VP, enhancing the precision and safety profile of PDT.

Altogether, these results reveal a strategic divergence in therapeutic use: VP-OA-NEs may be more suitable for light-independent or combinatorial therapies requiring inherent cytotoxicity, whereas VP-MG-NEs represent a promising platform for PDT where safety and spatial control are paramount. This emphasizes the importance of tailoring NEs composition to specific clinical goals, whether enhancing potency through carrier bioactivity or enabling selective, light-guided drug activation.

3.7. Photodynamic activity of free VP and VP-loaded NEs

To assess the light-dependent cytotoxicity of our formulations, SKOV3 cells were treated with free VP, VP-OA-NEs, and VP-MG-NEs. Later, they were exposed to two different irradiation intensities (1.0 and 3.3 mW cm^{-2}).

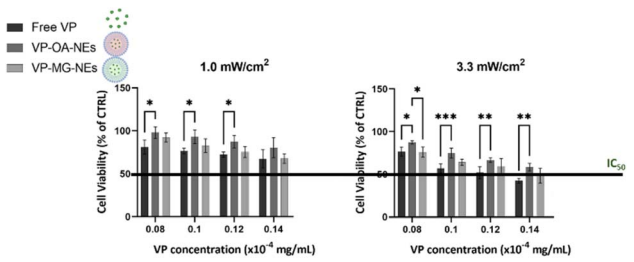

Fig. 14 Cell viability of SKOV-3 cells after light irradiation using two different intensities at increased concentrations of free VP, and VP loaded into NEs: VP-OA-NEs and VP-MG-NEs. Viability is expressed relative to untreated control cells (set at 100%). Differences between free VP and VP-loaded NEs were analyzed using two-way ANOVA. $^{**}p < 0.005$; $^{***}p < 0.0005$; $^{***}p < 0.0001$. Data represent mean ± SD ($n = 3$).

Analysis of the phototoxicity data demonstrated a pronounced dose- and light-intensity dependence; cell viability declined progressively with increasing VP concentrations (0.08–0.14 × 10^{-4} mg mL^{-1}) and higher irradiation intensities (Fig. 14). Importantly, a statistically significant difference was observed on the photodynamic therapy effect between VP-OA-NEs and free VP, while VP-MG-NEs and free VP showed similar performance ($IC_{50} \approx 0.14 \times 10^{-4}$ mg mL^{-1}) despite their negligible dark toxicity (see paragraph 3.5).

These results underscore the ability of MG-based NEs to protect cells from premature cytotoxicity while preserving photodynamic function, a property that aligns with previous reports demonstrating that VP-loaded lipid nanoparticles improve *in vivo* tumor targeting and reduce systemic side effects in ovarian cancer models. In the same study, the formulation effectively shielded healthy tissue from damage prior to light activation, thereby enhancing the therapeutic index, a principle directly supported by our VP-MG-NE data.[84]

Conversely, the reduced efficacy of VP-OA-NEs under light activation may reflect limited intracellular release or quenching effects stemming from OA interactions, or lower cellular uptake (Fig. 11), as seen in other formulations where carrier composition affects therapeutic performance.[85–87]

Taken together, our findings place VP-MG-NEs as promising platforms for photodynamic therapy in ovarian cancer: their excellent safety before light exposure, paired with retained phototoxic potency upon activation, supports optimal spatial and temporal control typical of PDT applications.

4. Conclusions

This study demonstrates the significant impact of oil phase selection on the formulation, cellular behavior, and therapeutic potential of verteporfin-loaded nanoemulsions. By comparing oleic acid and miglyol as oil cores, we found that VP-MG-NEs exhibited superior encapsulation efficiency, higher drug-loading capacity, improved stability, and greater uptake by SKOV-3 ovarian cancer cells.

Importantly, VP-MG-NEs allowed for the delivery of higher VP concentrations before inducing cytotoxic effects, suggesting that the MG-based formulation mitigates the intrinsic toxicity of the drug. In contrast, VP-OA-NEs induced cytotoxicity comparable to that of free VP at similar concentrations, even before light activation.

Photodynamic therapy experiments further confirmed that the therapeutic response was both dose- and light-dependent. VP-MG-NEs demonstrated significantly enhanced PDT efficacy compared to VP-OA-NEs, likely due to their higher intracellular accumulation and improved delivery profile under controlled photoactivation.

Altogether, these findings underscore that oil core composition is a critical parameter in the design of NE-based drug delivery systems. This work provides valuable insights for the rational development of safe and effective nanocarriers and

highlights the strong potential of VP-MG-NEs as a promising platform for photodynamic cancer therapy.

Author contributions

A. B. D.-I., C. C.-N., R. P.-C., M. A. and R. L.-L. conceptualization; A. B. D.-I., C. C.-N., R. P.-C., A. A. and L. F-V. methodology; L. F-V., M. E. V., and C. A.-R. validation; A. B. D.-I., C. C.-N., R. P.-C. formal analysis; L. F.-V., M. E. V., M. A. and A. B. D.-I. investigation; R. L.-L., C. C.-N. and I. V. E. A. K., resources; A. B. D.-I., L. F.-V. writing—original draft; R. P.-C., C. C.-N., R. L.-L., Lu-L., A. C. writing review and editing; L. F.-V., M. E. V., and A. B. D.-I. visualization; R. L.-L. and A. B. D.-I. supervision; A. B. D.-I. project administration; R. L.-L. funding acquisition.

Conflicts of interest

There are no conflicts to declare.

Data availability

The data supporting this article have been included as part of the SI. Supplementary information: (1) photoluminescence spectra, (2) VP-OA-NEs and OA-NEs physico-chemical characterization, after purification by Amicon ultra centrifugal devices, (3) physico-chemical characterization of OA-NEs and MG-NEs (size, polydispersity index, zeta potential, concetration) and Transmission Electron Microscopy images, (4) comparison between OA-NEs and VP-OA-NEs in terms of size and PDI before and after centrifugation, (5) table showing the obtained EE% as function of the injection mode, (6) numerical values of the real concentration of VP loaded into OA-NEs and MG-NEs because of the VP increment and corresponding changes in PDI, *Z*-potential, and size, (7) values of size, charge, and PDI for both types of NEs, VP-OA-NEs and VP-MG NEs, at the three different time points under the three different conditions, (8) number of particles per mL of the samples before and after filtration. See DOI: **https://doi.org/10.1039/d5na00496a**.

Acknowledgements

This work was supported by grant IN853B2018/03. Additional funding was provided by Aid from the Program for the Consolidation and Structuring of Research Units: Competitive Reference Groups (IN607A2024/05). I. V. and E. A. K. acknowledge support from the Italian Ministry of University (MUR) through the MINERVA grant—LuMIminesceNt Scintillating Heterostructures for Advanced Medical Imaging (grant no. H25E22000490006).

Notes and references

1 J. P. Martins, J. das Neves, M. de la Fuente, C. Christian, *et al.*, *Drug Delivery Transl. Res.*, 2020, **10**, 726–729.
2 C. Domingues, A. Santos, C. Alvarez-Lorenzo, A. Concheiro, I. Jarak, F. Veiga, I. Barbosa, M. Dourado and A. Figueira, *ACS Nano*, 2022, **16**, 7.
3 B. H. Alshammari, M. M. A. Lashin, M. Adil Mahmood, F. S. Al-Mubaddel, N. Ilyas and N. Rahman, *RSC Adv.*, 2023, **13**, 13735–13785.
4 W. Zhu, Z. Wei, C. Han and X. Weng, *Nanomaterials*, 2021, **11**(12), 3346.
5 S. E. Mendes Miranda, J. Lemos, F. Melo Ottoni, G. Dantas Cassali, D. M. Townsend, *et al.*, *Biomed. Pharmacother.*, 2024, **170**, 116054.
6 L. A. Gusmão, R. W. Köster and A. C. Tedesco, *Microchim. Acta*, 2024, **191**(10), 610.
7 Y. Chen, J. Yang, S. Fu and J. Wu, *Int. J. Nanomed.*, 2020, **24**(15), 9407–9430.
8 V. Secchi, A. Monguzzi and I. Villa, *Int. J. Mol. Sci.*, 2022, **23**, 8736.
9 I. Villa, C. Villa, R. Crapanzano, V. Secchi, M. Tawfilas, *et al.*, *ACS Appl. Mater. Interfaces*, 2021, **13**, 11.
10 Y. Wang, Y. Xu, J. Song, X. Liu, S. Liu, N. Yang, *et al.*, *Int. J. Nanomed.*, 2024, **19**, 5837–5858.
11 R. Saker, G. Regdon Jr and T. Sovány, *J. Drug Delivery Sci. Technol.*, 2024, **19**, 105979.
12 Z. M. D. Guo, G. Fernández-Varo, X. Zhang, S. Fu, *et al.*, *Mol. Pharm.*, 2022, **20**, 2.
13 H. Feracci, B. S. Gutierrez, W. Hempel and I. Segura Gil, *Front. Nanosci.*, 2012, **4**, 197–230.
14 M. Mehta, T. Anh Bui, X. Yang, *et al.*, *ACS Mater. Au*, 2023, **3**, 6.
15 T. T. Hoang Thi, E. J. A. Suys, J. Seok Lee, D. Ki Dong, *et al.*, *Vaccines*, 2021, **9**(4), 359.
16 H. Luiz, J. Oliveira Pinho and M. M. Gaspar, *Biomedicines*, 2023, **11**, 435.
17 M. Jaiswal, R. Dudhe and P. K. Sharma, *3 Biotech.*, 2015, **5**(2), 123–127.
18 Y. Liu, Y. Liang, J. Yuhong, P. Xin, J. L. Han, *et al.*, *Drug Des., Dev. Ther.*, 2024, **1**(18), 1469–1495.
19 R. J. Wilson, Y. Li, G. Yang and C.-X. Zhao, *Particuology*, 2022, **64**, 85–97.
20 M. Kumar, R. S. Bishnoi, A. K. Shukla and C. P. Jain, *Prev. Nutr. Food Sci.*, 2019, **24**(3), 225–234.
21 A. S. Alfutaimani, N. K. Alharbi, A. S. Alahmari, A. A. Alqabbani and A. M. Aldayel, *Int. J. Pharm.: X*, 2024, **8**, 100305.
22 Q. Liu, H. Huang, H. Chen, J. Lin and Q. Wang, *Molecules*, 2019, **24**, 4242.
23 S. Zhao, Z. Wang, X. Wang, B. Kong, *et al.*, *Foods*, 2023, **12**, 3183.
24 J. Hwang, J. Yeong Park, J. Kang, *et al.*, *Macromol. Rapid Commun.*, 2024, **45**, 2400480.
25 J. B. Đoković, S. Demisli, S. M. Savić, B. D. Marković, *et al.*, *Pharmaceutics*, 2022, **14**, 1666.
26 X. Hou and J. J. Sheng, *Geoenergy Sci. Eng.*, 2023, **221**, 211360.
27 R. López-Cabeza, M. Kah, R. Grillo, Z. Bílková and J. Hofman, *Nanoscale*, 2021, **13**, 5410–5418.
28 S. Kalepu and V. Nekkanti, *Acta Pharm. Sin. B*, 2015, **5**(5), 442–453.
29 X. Feng, Y. Sun, H. Tan, L. Ma, H. Dai and Y. Zhang, *Food Chem.*, 2023, **413**, 135653.

30 S. Bhattacharjee, *ACS Pharmacol. Transl. Sci.*, 2022, **5**(5), 278–298.
31 A. Alemi, J. Zavar Reza, F. Haghiralsadat, *et al.*, *J. Nanobiotechnol.*, 2018, **16**(1), 28.
32 H. Wang, W. Yan, Y. Sun and C. S. Yang, *Cancer Prev. Res.*, 2022, **15**(4), 233–245.
33 N. Carmona-Ule, C. Abuín Redondo, C. Costa, R. Piñeiro, *et al.*, *Mater. Today Chem.*, 2020, **16**, 100265.
34 C. Feng 1, Y. Wang, J. Xu, Y. Zheng, W. Zhou, Y. Wang and C. Luo, *Pharmaceutics*, 2024, **16**(12), 1582.
35 H. Liu, X. Jin, S. Liu, *et al.*, *J. Nanobiotechnol.*, 2025, **31**, 23.
36 US FDA label for Visudyne®.
37 D. Newman, *Eye*, 2016, **30**, 202–210.
38 G. M. Demirbolat, *et al.*, *Colloids Surf., B*, 2021, **204**, 111795.
39 N. Kundu, D. Mondal and N. Sarkar, *Biophys. Rev.*, 2020, **12**, 1117–1131.
40 N. Buss, P. Ryan, T. Baughman, D. Roy, C. Patterson, C. Gordon and R. Dixit, *J. Appl. Toxicol.*, 2018, **38**, 10.
41 T. Michy, T. Massias, C. Bernard, L. Vanwonterghem, M. Henry, M. Guidetti, G. Royal, J. Luc Coll, I. Texier, V. Josserand and A. Hurbin, *Cancers*, 2019, **11**(11), 1760.
42 N. Shah, S. Reddy Soma, M. Bortei Quaye, D. Mahmoud, S. Ahmed, A. Malkoochi and G. Obaid, *ACS Appl. Bio Mater.*, 2024, **7**, 7.
43 T. Mendes, A. Granja and S. Reis, *Mater. Adv.*, 2024, **5**, 1137–1146.
44 C. Kent, Molecular and Cell Biology of Lipids, *Biochim. Biophys. Acta*, 2005, **1733**(1), 53–66.
45 B. N. Olsen, A. A. Bielska, T. Lee, M. D. Daily, *et al.*, *Biophys. J.*, 2013, **105**(8), 1838–1847.
46 A. Abolfazl, R. Rezaei-Sadabady, S. Davaran, *et al.*, *Nanoscale Res. Lett.*, 2013, **8**(1), 102.
47 J. Singh Negi, *Characterization and Biology of Nanomaterials for Drug Delivery*, ch. 6, 2019, pp. 137–163.
48 P. Ha-Lien Tran, T. Truong-Dinh Tran and B. J. Lee, *Int. J. Pharm.*, 2013, **455**(1–2), 235–240.
49 J. W. Lui, S. Xiao, K. Ogomori, J. E. Hammarstedt, E. C. Little and D. Lang, *J. Cancer*, 2019, **10**(1), 1–10.
50 **https://www.ema.europa.eu/en/documents/product-information/visudyne-epar-product-information_en.pdf**.
51 K. F. Sergey, R. Khusnutdinov, A. Murmiliuk, W. Inam, L. Ya. Zakharova, H. Zhang and V. V. Khutoryanskiy, *Mater. Horiz.*, 2023, **10**, 5354–5370.
52 N. Carmona-Ule, N. Gal, C. Abuín Redondo, *et al.*, *Bioengineering*, 2022, **9**(8), 380.
53 S. Parashar, C. Chauhan, A. Rajasekharan, J. Rautela, T. Jain and K. Raza, *Front. Bioeng. Biotechnol.*, 2022, **10**, 833456.
54 J. Weng, H. H. Y. Tong and S. F. Chow, *Pharmaceutics*, 2020, **12**, 732.
55 E. Johnsen, O. K. Brandtzaeg, T. Vehus, *et al.*, *J. Pharm. Biomed. Anal.*, 2016, **20**(120), 106–111.
56 L. Xu, X. Wang, Y. Liu, G. Yang, *et al.*, *NanoBiomed Res.*, 2022, **2**, 2100109.
57 D. Quintanar-Guerrero, E. Allémann, E. Doelker, *et al.*, *Colloid Polym. Sci.*, 1997, **275**, 640–647.
58 M. A. Schubert and C. C. Müller-Goymann, *Eur. J. Pharm. Biopharm.*, 2003, **55**, 125–131.
59 H. Hassanzadeh, M. Alizadeh, R. Hassanzadeh and B. Ghanbarzadeh, *Food Sci. Nutr.*, 2022, **10**(5), 1613–1625.
60 R. V. Tonon, R. B. Pedro, C. R. F. Grosso and M. D. Hubinger, *Drying Technol.*, 2012, **30**(13), 1491–1501.
61 A. Mazloom and N. Farhadyar, *Researcher*, 2014, **6**(4), 32–36.
62 C. Viegas, A. B. Patrício, J. M. Prata, A. Nadhman, P. K. Chintamaneni and P. Fonte, *Pharmaceutics*, 2023, **15**(6), 1593.
63 N. E. Eleraky, M. M. Omar, H. A. Mahmoud and H. A. Abou-Taleb, *Pharmaceutics*, 2020, **12**, 451.
64 A. M. Jörgensen, C. Steinbring, D. Stengel, D. To, P. Schmid and A. Bernkop-Schnürch, *Adv. Healthcare Mater.*, 2023, **12**(31), 2302034.
65 M. H. Zulfakar, H. Pubadi, S. I. Ibrahim and N. M. Hairul, *J. Oleo Sci.*, 2024, **73**(3), 293–310.
66 S. S. Rane and B. D. Anderson, *Adv. Drug Delivery Rev.*, 2008, **60**(6), 638–656.
67 Y. Singh, J. Gopal Meher, K. Raval, F. A. Khan, M. Chaurasia, N. K. Jain and M. K. Chourasia, *J. Controlled Release*, 2017, **252**, 28–49.
68 V. Katev, Z. Vinarov and S. Tcholakova, *Eur. J. Pharm. Sci.*, 2021, **159**, 105733.
69 S. Kalepu and V. Nekkanti, *Acta Pharm. Sin. B*, 2015, **5**(5), 442–453.
70 J. Musakhanian, J. D. Rodier and M. Dave, *AAPS PharmSciTech*, 2022, **23**, 151.
71 M. Danaei, M. Dehghankhold, S. Ataei, F. Hasanzadeh, R. Javanmard, A. Dokhani, S. Khorasani and M. R. Mozafari, *Pharmaceutics*, 2018, **10**(2), 57.
72 A. C. Anselmo and S. Mitragotri, *Adv. Drug Delivery Rev.*, 2017, **108**, 51–67.
73 S. Li, H. Yuan, L. Li, Q. Li, P. Lin and K. Li, *Antioxidants*, 2025, **14**(2), 201.
74 M. Danielli, L. Perne, E. Jarc Jovičić and T. Petan, *Front. Cell Dev. Biol.*, 2023, **27**(11), 1104725.
75 S. S. Funari, F. Barceló and P. V. Escribá, *J. Lipid Res.*, 2003, **44**(3), 567–575.
76 S. Okonogi, P. Phumat, S. Khongkhunthian, P. Chaijareenont, T. Rades and A. Müllertz, *Pharmaceutics*, 2021, **13**, 167.
77 R. Sellers, M. Antman, J. Phillips, *et al.*, *Drug Chem.*, 2005, **28**(4), 423–432.
78 Y. Yalçın, I. O. Tekin and R. S. Tığlı Aydın, *J. Biomater. Nanobiotechnol.*, 2021, **12**, 49–56.
79 M. Janik-Hazuka, J. Szafraniec-Szczęsny, K. Kamiński, J. Odrobińska and S. Zapotoczny, *Int. J. Biol. Macromol.*, 2020, **164**, 2000–2009.
80 S. A. Dragulska, Y. Chen, M. T. Wlodarczyk, M. Poursharifi, P. Dottino, *et al.*, *Bioconjugate Chem.*, 2018, **29**(8), 2514–2519.
81 A. Tanaudommongkon, I. Tanaudommongkon, P. Prathipati, J. Nguyen and X. Dong, *J. Nanosci. Nanotechnol.*, 2017, **17**(6), 3920–3926.
82 R. M. Khalil, A. Abd-Elbary, M. A. Kassem, M. M. Ghorab and M. Basha, *Pharm. Dev. Technol.*, 2013, **19**(3), 304–314.
83 K. Dziza, E. Santini, L. Liggieri, E. Jarek, M. Krzan, T. Fischer and F. Ravera, Interfacial Properties and Emulsification of

Biocompatible Liquid-Liquid Systems, *Coatings*, 2020, **10**, 397.
84 T. Michy, T. Massias, C. Bernard, L. Vanwonterghem, M. Henry, M. Guidetti, *et al.*, *Cancers*, 2019, **11**(11), 1760.
85 S. Moghassemi, A. Dadashzadeh, R. B. Azevedo and C. A. Amorim, *J. Controlled Release*, 2022, **351**, 164–173.
86 T. Mendes, A. Granja and S. Reis, *Mater. Adv.*, 2024, **5**, 1137–1146.
87 J. A. Quinlan, C. T. Inglut, P. Srivastava, I. Rahman, *et al.*, *Adv. Sci.*, 2024, **11**(17), 2302872.